JET INTERACTION IN A HYPERSONIC FLOW: A COMPARISON BETWEEN PLIF THERMOMETRY AND COMPUTATIONAL SIMULATION

Stefan Brieschenk*, **Rolf M. Gehre***, **Vincent Wheatley***, **Russell R. Boyce***, **Harald Kleine****and **Sean O'Byrne****

***Centre for Hypersonics,**
The University of Queensland,
Brisbane, QLD 4072, Australia,
****School of Engineering and Information Technology,**
The University of New South Wales,
The Australian Defence Force Academy,
Canberra, ACT 2600, Australia
s.brieschenk@uq.edu.au

Keywords: *jet interaction, hypersonic flow, planar laser-induced fluorescence (PLIF) thermometry, nitric oxide PLIF, Reynolds-Averaged Navier-Stokes simulation*

Abstract

Two-dimensional temperature measurements of the interaction between a sonic H_2 jet injected into a hypersonic air-crossflow are compared to Reynolds-Averaged Navier-Stokes (RANS) simulations. The temperature measurements were obtained using the planar laser-induced fluorescence (PLIF) technique on the nitric oxide molecule. The experimental setup consists of a $9°$ compression ramp and a single, 1.6-mm-diameter fuel injector, angled at $81°$ to the crossflow. The RANS simulation shows good general agreement with the ensemble-averaged experimental data, but discrepancies are significant in regions where large-scale vortex structures dominate the unsteady flow.

1   Introduction

The physics of the interaction of gaseous jets with high-supersonic crossflows is of great importance for maneuvering access-to-space and re-entry vehicles as well as for fuel injection in air-breathing, supersonic combustion engines such as scramjets. Experiments on jet interaction typically focus on the determination of shock positions and fuel penetration heights using density-sensitive visualisation techniques as well as wall pressure and heat-flux measurements. While these surface data give a good indication of the flow properties at the wall, the evaluation of numerical codes require more complete experimental data, preferably fluid properties in the jet interaction region, rather than properties directly at the wall. This study uses the planar laser-induced fluorescence (PLIF) technique to determine spatially resolved temperatures in the centreplane of a jet interaction in a hypersonic flow. The planar laser-induced fluorescence technique is a well established method to non-intrusively visualise a gaseous flow and measure its temperature, velocity or species concentrations [1]. These experimental data are then compared to computational fluid dynamic (CFD) simulations using the Reynolds-Averaged Navier-Stokes (RANS) equations.

The principle behind the PLIF technique is the laser-induced fluorescence process, where

atom/molecule-bound electrons are elevated to higher energy levels by absorbing photons with energies similar to the energy gap between the two energy levels. A narrow-bandwidth laser is used to supply photons with equal energies. After a short residence time in the excited state, the electrons undergo radiative de-excitation, i.e. fall back into their ground states, by emitting photons. The emitted light typically has a wavelength longer than that of the exciting laser beam and hence one observes fluorescence. The fluorescence signal is a function of the atom/molecule number densities as well as their temperatures by simple Boltzmann statistics. In the PLIF thermometry technique, two-dimensional temperature fields are generated from two-dimensional fluorescence fields.

Assuming that both measured transitions $L1$ and $L2$ belong to the same vibrational ground state and that the same optical system is used to collect the fluorescence, the rotational temperature T_{rot} in the linear (weak excitation) two-line fluorescence regime may be expressed as [1, 2, 3, 4, 5]

$$T_{rot} = \frac{F_{J''}^{L2} - F_{J''}^{L1}}{k_B \, ln \left(\frac{2J_{L2}'' + 1}{2J_{L1}'' + 1} \cdot A \cdot C_A + C_B \right)}$$

with

$$A = \frac{HL_{L2} \, E_{\nu_{L2}}^{las} \, g_n^{L2} \, \Phi_F^{L2} \, S_{f_{lin}}^{L1} \, \chi_i^{L2}}{HL_{L1} \, E_{\nu_{L1}}^{las} \, g_n^{L1} \, \Phi_F^{L1} \, S_{f_{lin}}^{L2} \, \chi_i^{L1}}$$

where J'' is the ground-state rotational quantum number, $F_{J''}$ [cm^{-1}] the ground-state rotational energy of the electronic transition and k_B [J K^{-1}] the Boltzmann constant. The ratio of the rotational line strength factors (Hönl-London factors) HL_{L2}/HL_{L1} are known for the chosen spectral transitions. If the same probing laser is used for both measurements, the ratio of laser spectral energy densities $E_{\nu_{L2}}^{las}/E_{\nu_{L1}}^{las}$ becomes unity. The effects of line broadening and shifting cancel if both transitions are affected to a similar degree, and g_n^{L2}/g_n^{L1} becomes unity unless doublet transitions are used. The ratio of fluorescence efficiencies Φ_F^{L2}/Φ_F^{L1} may differ from unity due to temperature-dependent quenching, saturation or absorption. Interference with neighbouring transitions or radiative trapping can influence the ratio of collected fluorescence signals $S_{f_{lin}}^{L1}/S_{f_{lin}}^{L2}$. The two-line PLIF thermometry technique requires the experiment to be repeated at least twice to allow one to probe two different energy states. In a turbulent mixing flow, the fluorescent species' mole fractions χ_i^{L2} and χ_i^{L1} may differ between individual experiments. If the ratio χ_i^{L2}/χ_i^{L1} cannot be measured, a number of experiments can be performed to average out fluctuations in χ_i. C_A and C_B are correction parameters which may be used to compensate for systematic errors due to laser absorption, non-linear ensemble-averaging or any other systematic error source that can be quantified.

2 Experimental Test Facility and Model

The NO-PLIF thermometry measurements were conducted in the T-ADFA free piston shock tunnel at the University of New South Wales, Australian Defence Force Academy. Only a brief description of the experimental setup is given here, more detail can be found elsewhere [5]. The facility is operated in reflected-shock mode, thereby generating nitric oxide (NO) upon stagnation of the flow in the nozzle reservoir, which is then chemically frozen in the expanding nozzle flow. A conical nozzle with an area ratio of 256 and a 12.7-mm nozzle throat is used to generate the freestream. The total flow properties are determined by solving the inviscid normal shock equations [6] for the initial and reflected shock waves using the ESTC code [7] with the measured shock speeds and measured total pressure in the nozzle reservoir. The freestream properties are calculated using the one-dimensional, inviscid nozzle code STUBE [8]. Furthermore, a reduced nozzle area ratio is used for the STUBE calculation to account for the displacement thickness of the developing boundary layer, which achieves best agreement with the measured pitot pressure. STUBE accounts for thermal and chemical non-equilibrium in the nozzle flow. The flow properties determined by these two codes

are shown in Tab. 1. The thermal equilibrium properties in Tab. 1 are found by setting the thermal non-equilibrium temperatures that are calculated by STUBE into equilibrium. The chemical freezing in the rapid nozzle expansion results in a volume fraction of 1.3 % NO in the freestream. Fig. 1 shows the freestream temperatures as functions of time after shock reflection determined using this approach. The experimental arrangement of the model used for the jet injection study is shown in Fig. 2. A 1.6-mm-diameter port hole injector is located 120 mm downstream of the leading edge of the model, angled at 81° to the flow on the compression ramp. Hydrogen is injected with a plenum pressure of 2075 kPa.

The NO molecules are excited from their ground electronic state $X^2\Pi$ into their first electronic state $A^2\Sigma^+$ via vibrational $v'' \leftarrow v'\, 0 \leftarrow 0$ band transitions. The experimental setup of the NO PLIF system is shown in Fig. 3. A Lambdaphysik Scanmate II dye laser is used together with a frequency doubler to generate tunable UV radiation between 224 nm and 228 nm at pulse energies of the order of 800 μJ. The dye laser is pumped using the third harmonic of a Spectra-physics GCR4 Nd:YAG laser at 355 nm. The dye laser is operated with Coumarin 2 dye (LC 4500, dissolved in methanol) on grating order 7 without an intra-cavity etalon. A small portion of the

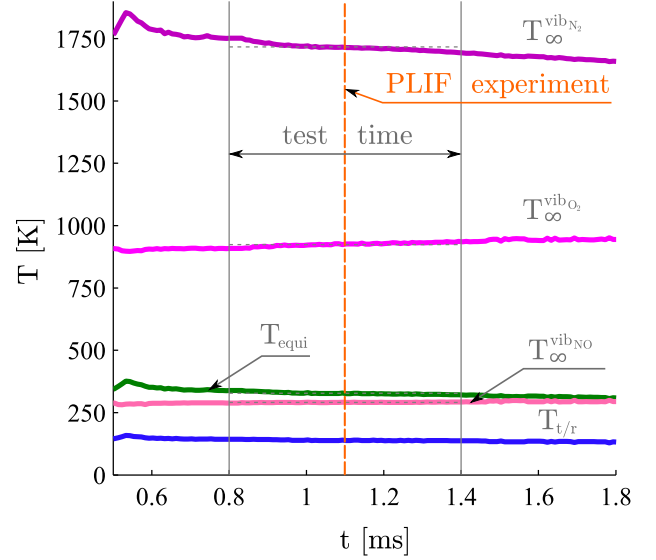Fig. 1 : Freestream temperatures, calculated using the ESTC and STUBE codes, plotted against time.
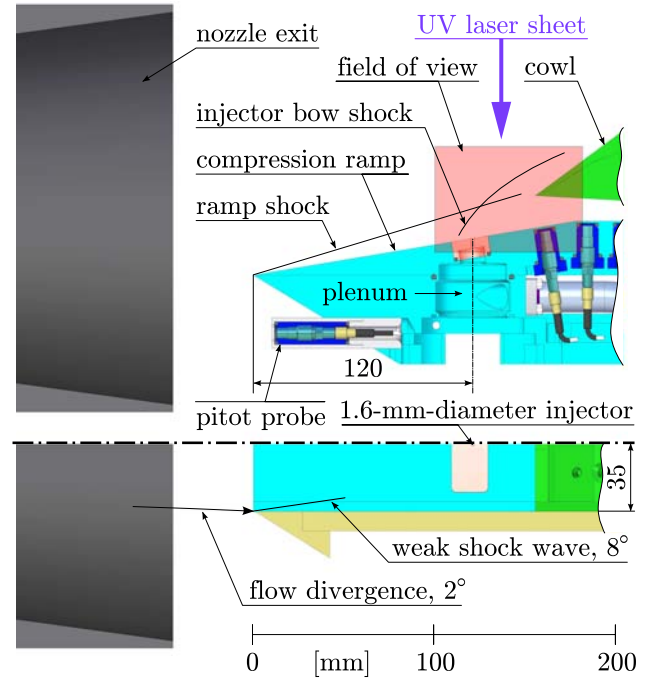
Fig. 2 : Experimental arrangement (to scale)

total flow properties			
h_0 [MJ/kg]	2.5	$T_{\infty,NO}^{vib}$ [K]	295
T_0 [K]	2140	p_∞[Pa]	720
p_0 [MPa]	13	ρ_∞[g/m^3]	19
freestream properties		**injector flow**	
u_∞[m/s]	2075	p_{plenum} [kPa]	2075
M_∞^{equi}[-]	5.7	T^* [K]	231
$M_\infty^{t/r}$[-]	9.0	p^* [kPa]	1092
T_∞^{equi} [K]	325	ρ^* [kg/m^3]	1.14
$T_\infty^{t/r}$ [K]	130	a^* [m/s]	1161
T_{∞,N_2}^{vib} [K]	1740	γ_{avg} [-]	1.4
T_{∞,O_2}^{vib} [K]	930	C_d [-]	0.89
		$\dot{m}$ [g/s]	2.4

Table 1: Flow condition parameters, averaged over a 1 ms test time. The superscripts ^{equi} and $^{t/r}$ represent equilibrium and transrotational nonequilibrium conditions, respectively.

UV laser beam is tapped off the main beam (using a fused silica plate) for frequency calibration. Frequency calibration is performed using a gas cell filled with pure NO at a pressure of 500 Pa. Fluorescence in the gas cell is captured using a photomultiplier tube equipped with a Schott UG 5 glass filter. The laser sheet is formed us-

ing two converging lenses, a 30-mm-focal-length cylindrical and a 1000-mm-focal-length spherical lens. The height of the sheet-forming lenses relative to the model is set such that the width of the laser sheet measures 1 mm on the surface of the model. A fused silica plate is used as a beam splitter to record the intensity distribution of the UV laser sheet by guiding the sheet onto a dye cell with a methanol/Rhodamine 6G dye solution. A MicroPix 1024 CCD camera captures the sheet profile and allows the PLIF images to be corrected for spatial sheet-nonuniformity and run-to-run deviations in laser energy. The electronically excited NO molecules radiatively decay with unquenched fluorescence lifetimes of 206 ns [9] for $v' = 0$ state transitions and 198 ns for collisionally populated $v' = 1$ state transitions. The majority of the fluorescence [10] is typically caused near 237 nm $(1 \leftarrow 0)$, 247 nm $(2 \leftarrow 0)$, 259 nm $(3 \leftarrow 0)$ and 227 nm $(0 \leftarrow 0)$. Fluorescence from the collisionally populated $v' = 1$ state is caused near 215 nm $(0 \leftarrow 1)$ and to a lesser extent near 224 nm $(1 \leftarrow 1)$. The UV fluorescence is captured using a Princeton Instruments intensified charge-coupled device (ICCD-576-S/1) camera with a UV-Nikkor 105 mm $f/4.5$ lens. A Schott UG 5 glass filter (thickness 2 mm) is used to spectrally filter the fluorescence signal from flow luminosity. The ICCD camera gate is opened 10 ns before the arrival of the laser sheet in the test section, to capture all of the available fluorescence signal, and is exposed for 200 ns.

2.1 Probed Electronic Transitions

The temperature sensitivity and uncertainty of the two-line thermometry technique depend on the selected electronic transitions. The relative population of electronic transitions within the same vibrational energy level is determined by Boltzmann statistics. The chosen electronic transitions need to have a large energy spacing and need to be populated sufficiently to yield fluorescence signals that are within the dynamic range of the detection system. For the temperatures to be determined with acceptable uncertainty, three electronic transitions have
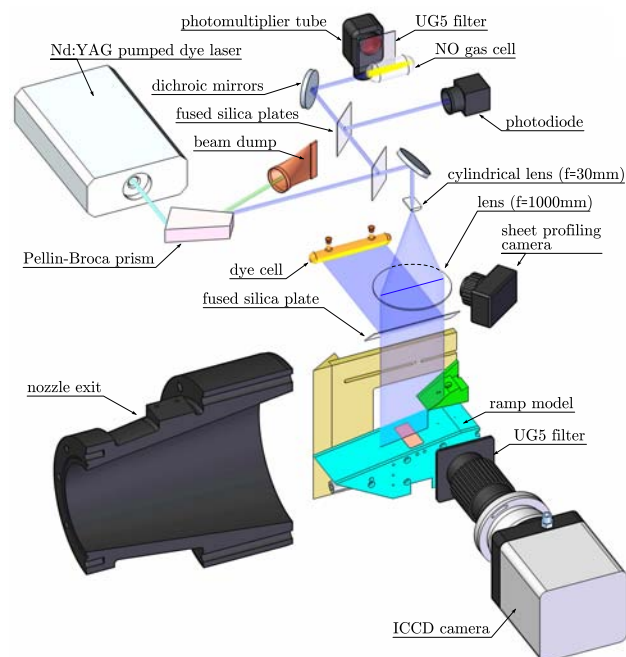

Fig. 3 : NO PLIF system with compression ramp model

been probed. Doublet transitions are chosen for the thermometry measurements performed here in an attempt to increase fluorescence signals. The spectral parameters of the transitions that were selected for the temperature measurements [5] are given in Tab. 2. All transitions are $v'' \leftarrow v'$ $0 \leftarrow 0$ transitions with a vibrational energy of $G_v'' = 948.66 \, \text{cm}^{-1}$. The rotational energy levels N in the NO molecule are split into a fine structure due to spin-orbit interaction. Each rotational energy level is further split into a hyperfine structure by Λ-doubling, due to the interaction between nuclei and electrons. The ground-state populations of these transitions as functions of temperature are shown in Fig. 4. The temperature dependence of the signal ratios is shown in Fig. 5. Transrotational temperatures below 380 K are calculated from the signal ratio between the $^{R}R_{11}{}^{R}Q_{21}(1.5)$ and the $^{Q}Q_{22}{}^{Q}R_{12}(13.5)$ transitions whereas temperatures above 380 K are determined using the $^{Q}Q_{22}{}^{Q}R_{12}(13.5)$ and $^{Q}Q_{22}{}^{Q}R_{12}(32.5)$ transitions. The threshold temperature is chosen such that the collected fluorescence signals are within the dynamic range of the detection system. For each of the three electronic

Spectral line	J'' [−]	J' [−]	splitting: fine $A \leftarrow X$	-hyperfine $A \leftarrow X$
$^{Q}Q_{22}$	32.5	32.5	$\mathbb{F}_2 \leftarrow \mathbb{F}_2$	$-f \leftarrow +e$
$^{Q}R_{12}$	32.5	33.5	$\mathbb{F}_1 \leftarrow \mathbb{F}_2$	$-e \leftarrow +e$
$^{Q}Q_{22}$	13.5	13.5	$\mathbb{F}_2 \leftarrow \mathbb{F}_2$	$-f \leftarrow +e$
$^{Q}R_{12}$	13.5	14.5	$\mathbb{F}_1 \leftarrow \mathbb{F}_2$	$-e \leftarrow +e$
$^{R}R_{11}$	1.5	2.5	$\mathbb{F}_1 \leftarrow \mathbb{F}_1$	$+e \leftarrow -e$
$^{R}Q_{21}$	1.5	1.5	$\mathbb{F}_2 \leftarrow \mathbb{F}_1$	$+f \leftarrow -e$

Spectral line	ν_0 [cm^{-1}]	F_J [cm^{-1}]	$B_{J'}^{J''}(B_{12})$ [$\frac{m^2}{Js}$]
$^{Q}Q_{22}$	44439.560	1921.16	8.908×10^8
$^{Q}R_{12}$	44439.470	1921.16	7.706×10^7
$^{Q}Q_{22}$	44161.105	394.93	7.369×10^8
$^{Q}R_{12}$	44161.067	394.93	1.478×10^8
$^{R}R_{11}$	44205.922	−54.86	3.349×10^8
$^{R}Q_{21}$	44205.929	−54.86	5.546×10^8

Table 2: Parameters of spectral lines used for the NO PLIF thermometry experiments [5]; B_{12} refers to the Einstein coefficient for stimulated absorption; $\mathbb{F}$ refers to spin-orbit interaction splitting; e and f refer to Λ-type splitting
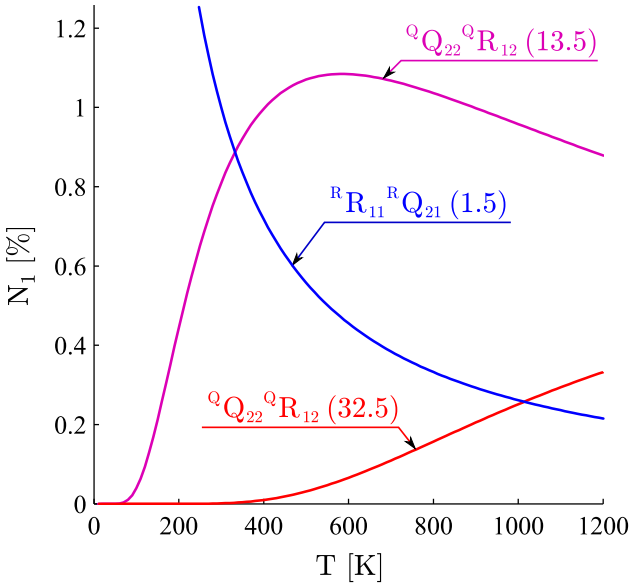

Fig. 4 : Ground-state populations N_1 of electronic transitions plotted against transrotational temperature [5].
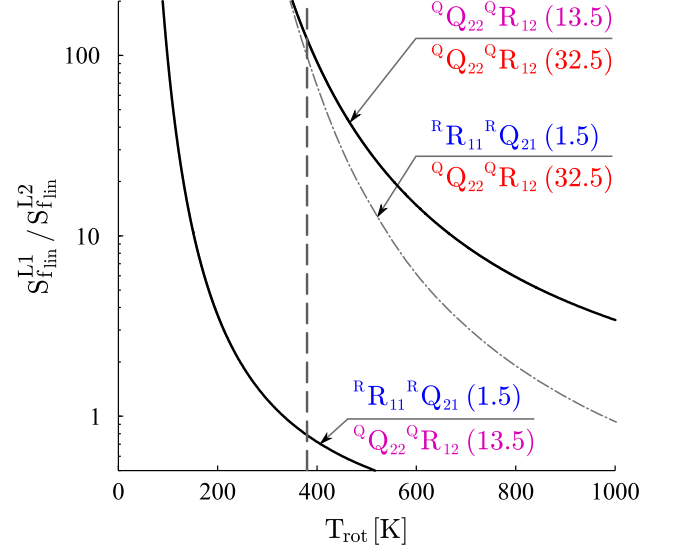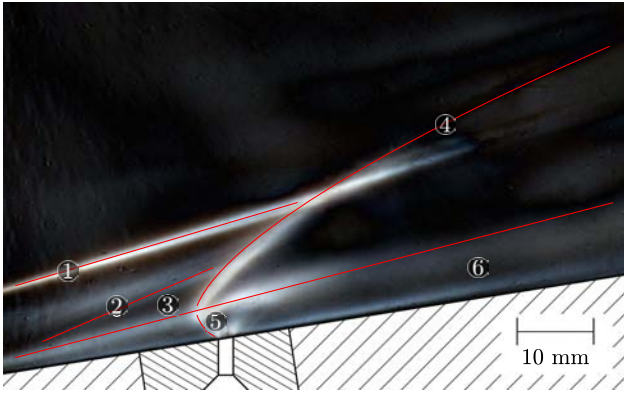

Fig. 5 : Temperature dependence of signal ratios. At $T < 380\,\text{K}$, the flow temperature is determined using the signal ratio between the $^{Q}Q_{22}{}^{Q}R_{12}(13.5)$ and the $^{R}R_{11}{}^{R}Q_{21}(1.5)$ transitions. At $T > 380\,\text{K}$, the flow temperature is determined using the signal ratio between the $^{Q}Q_{22}{}^{Q}R_{12}(13.5)$ and the $^{Q}Q_{22}{}^{Q}R_{12}(32.5)$ transitions.

transitions. While these transitions have a larger energy spacing $F_{J''}^{L2} - F_{J''}^{L1}$, the signal from the $^{Q}Q_{22}{}^{Q}R_{12}(13.5)$ transition is significantly stronger than the signal from the $^{R}R_{11}{}^{R}Q_{21}(1.5)$ transition and the $^{Q}Q_{22}{}^{Q}R_{12}(13.5)$ transition. Furthermore, the signal of the $^{R}R_{11}{}^{R}Q_{21}(1.5)$ transition is strongly affected by absorption in the freestream. The absorption of this electronic transition has a small effect on temperatures below 380 K, but a more significant effect on temperatures above 380 K if the signal ratio between the $^{R}R_{11}{}^{R}Q_{21}(1.5)$ and $^{Q}Q_{22}{}^{Q}R_{12}(32.5)$ transitions is used for the temperature measurement (Fig. 5). Absorption is accounted for through the calibration value C_A in Equation 1. Taking the effective absorption length as half the nozzle diameter, C_A is estimated as $C_A = 2.3 \pm 0.3$ for the temperature measurements in the freestream.

2.2 Experimental Results

The measured rotational temperature map of the flowfield is shown in Fig. 7. Uncertainties aris-

transitions, seven experiments were conducted. As seen from Fig. 5, temperatures above 380 K may also be determined using the signal ratio between the $^{R}R_{11}{}^{R}Q_{21}(1.5)$ and $^{Q}Q_{22}{}^{Q}R_{12}(32.5)$

1	leading edge shock	4	interaction bow shock
2	separation shock	5	jet incident shock
3	separated boundary layer	6	boundary layer

Fig. 6 : Schlieren image of flowfield, for qualitative comparison only, injector diameter here is 2 mm and fuel plenum pressure is 832 kPa.

ing from the signal fluctuations are plotted in Fig. 8. Areas where the NO mole fractions are too low for accurate temperature measurements are greyed-out in these figures. The underexpanded hydrogen fuel jet expands into the crossflow, which generates the jet interaction shock and separates the upstream boundary layer as seen in the schlieren image depicted in Fig. 6. The cold hydrogen jet has a significant cooling effect on the flow and temperatures in the fuel mixing region are typically < 300 K. Measurement uncertainties are typically 10–15 % in the freestream and 15–25 % in the regions behind the leading edge shock wave and the jet interaction shock wave. Measurement uncertainties are higher in the fuel mixing region and the separated region upstream of the fuel injection port due to low fluorescence signals as well as local flow unsteadiness.

2.3 RANS simulations

The numerical simulations were performed using the US3D code, which was developed at the University of Minnesota [11]. A hybrid structured/unstructured finite volume scheme is employed to solve the compressible Navier-Stokes equations. Turbulence is modeled using the Spalart-Allmaras one-equation model [12].
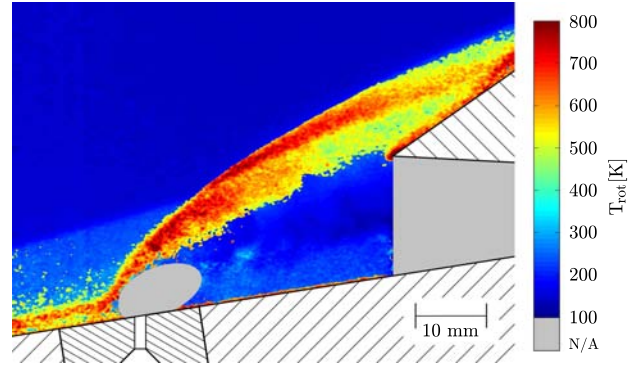

Fig. 7 : Temperature map constructed from the $^{Q}Q_{22}\,^{Q}R_{12}\,(13.5)$ to $^{R}R_{11}\,^{R}Q_{21}\,(1.5)$ signal ratios (for $T_{rot} \leq 380$ K) and $^{Q}Q_{22}\,^{Q}R_{12}\,(32.5)$ to $^{Q}Q_{22}\,^{Q}R_{12}\,(13.5)$ signal ratios (for $T_{rot} > 380$ K).
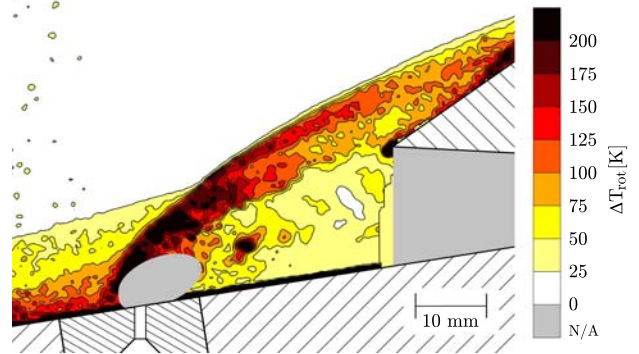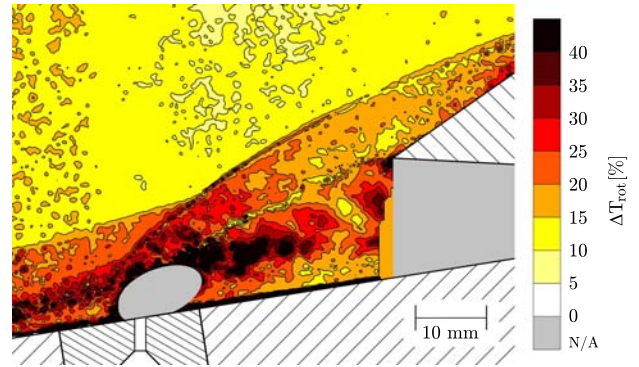

Fig. 8 : Relative (top) and absolute (bottom) temperature uncertainty maps corresponding to the temperature map shown in Fig. 7.

Two RANS simulations were performed, one for the nozzle flow to account for the divergence and flow structure of the freestream and one for the jet interaction experiment. A two-dimensional axisymmetric RANS simulation was performed to determine the freestream properties and profiles that are generated by the con-

ical shock-tunnel nozzle. The RANS computation includes a two-temperature model to account for the thermal non-equilibrium in the nozzle flow. A 5 species, 5 equation air reaction scheme was employed in the computations [13]. Since the shock-tunnel test time is less than $1ms$, the wall temperature is assumed to be constant, with $T_{wall} = 293$ K. Furthermore, to resolve the developing boundary layer accurately the first wall-normal cell height ranges from 15 nm in the nozzle throat to 10μm at the nozzle exit, ensuring their y^+ values are smaller than 1. The resulting nozzle mesh contains $435,600$ cells.

The RANS simulation has been initialised with the stagnation condition provided in table 1. Fig. 9 shows the Mach number distribution within the nozzle with the static pressure distributions superimposed at $x = 0.3$ m, 0.5 m, 0.7 m and 0.9 m. Since the transition point of the boundary layer from laminar to turbulent is unknown, several simulations with different tripping locations have been performed. The best agreement with the available pitot pressure data can be achieved if the boundary layer trips at $x = 0.4$ m. A weak shock wave, originating from the tripping location can be seen in Fig. 9. The flow quantities within the nozzle core flow can, however, still be assumed to be uniformly distributed in the radial direction. Tab. 3 provides the averaged freestream properties generated with the RANS simulation, which agrees reasonably well with the ones calculated from STUBE. The nozzle RANS results are used as an inflow for the injector simulation. The divergence angle of the freestream varies by $3°$ over the entire inflow domain, influencing the jet interaction characteristics, making a CFD nozzle simulation essential.

As mentioned before, the nozzle outflow is interpolated onto the inflow domain for the jet interaction simulation. The experiment itself is simulated using a three-dimensional RANS simulation. However, only the compression ramp and the injector are modeled, the upper cowl is not included in the simulation. Furthermore, the weak shock wave and corner separation originating from the sidewalls have no effect on the ex-

periment since these flow structures intersect the model center line downstream of the flow visualisation region. Therefore, only a small spanwise region near the centerline, $z = \pm 5$ mm, has to be finely resolved. The remaining domain under resolves the flow features due to its decreased spanwise resolution, which is why the sidewalls are treated as slip walls. The final 3D mesh has a total of 14,530,514 cells and the first wall-normal grid spacing is 0.1μm, resulting in y^+ smaller than 1.

This simulation does not employ the two-temperature thermal non-equilibrium model, due to shortcomings of the two-temperature model in mixing regions. Since the flow stays in most regions supersonic ($M \geq 3.5$, $u \geq 1750$ m/s) and relatively cool for a large part of the experimental domain ($T \leq 800$ K), the vibrational temperature would be close to frozen. Analysing the nozzle simulation indicates that the condition for thermal freezing is fulfilled at translational temperatures below roughly $T = 750$ K and flow velocities above $u = 1725$ m/s. Since large regions of the injection interaction flow field exhibit lower translational temperatures and higher flow velocities compared to the afore mentioned ones, the assumption of a thermally frozen state seems reasonable, which indicates an insignificant influence of the vibrational temperature on the results. Therefore, the elevated vibrational energy, present in the outflow of the nozzle simulation, is neglected, reducing the total energy of the freestream by roughly 5 %. On the other hand, including the vibrational energy into the translational-rotational energy would increase

freestream properties	
u_∞[m/s]	2063
$M_\infty^{t/r}$[-]	8.7
$T_\infty^{t/r}$ [K]	140
T_∞^{vib} [K]	1238
p_∞ [Pa]	675
ρ_∞ [g/m^3]	16.7

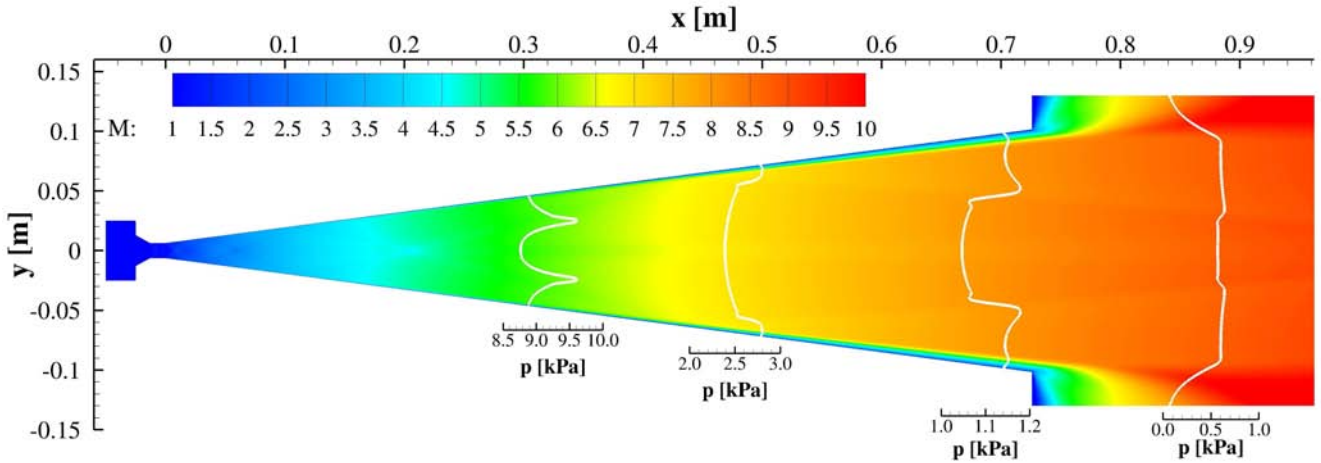**Table 3**: Freestream flow conditions extracted from the nozzle RANS simulation

Fig. 9 : Mach number contours within the nozzle with the static pressure distributions superimposed at streamwise locations $x = 0.3$ m, 0.5 m, 0.7 m and 0.9 m

the translational temperature, which would cause a mismatch of the freestream temperature and the shock alignment. Therefore, disregarding the vibrational energy is a reasonable choice, though still not completely accurate. The chemistry model used is the 5 species air-reaction scheme [13], which was employed for the nozzle simulation as well. Additionally, hydrogen has been added as a species which acts as an inert gas, only taking part in the dissociation reactions for N_2, O_2 and NO as a third body. Thus, hydrogen does not react with any of the other species in the simulation. This assumption is reasonable since the pressures and temperatures at the jet interaction are for a large part of the domain below 25 kPa and 800 K, respectively, which is too low for combustion [14]. There is, however, the possibility of radical production in regions where the flow is almost stagnated. The effect of these radicals on the temperature distribution is assumed to be negligible, but further reacting flow simulations will be conducted in the future to investigate this issue.

Fig. 10 shows the temperature distribution in the RANS simulation for the experimental field of view. Not shown is a large part of the leading edge ramp, which is depicted in Fig. 2. The oblique shock wave originating from the leading edge of the experimental arrangement draws a relative angle of $6°$ with the ramp surface. The
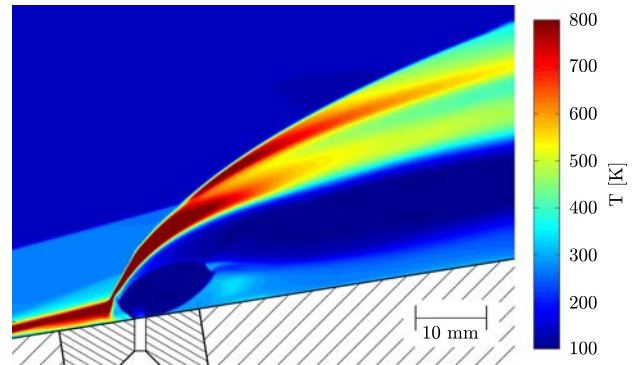

Fig. 10 : Temperature distribution in RANS simulation.

temperatures increase from 140 K to 300 K over the shock. The oblique shock wave enters Fig. 10 on the lower left hand side as indicated by the temperature increase. Agreement with the experimental data in terms of the location of the leading edge shock wave was found after including the leading edge radius into the computational model. Testing in shock tunnel facilities exposes the model to debris that collide with the model after the test time with velocities that can exceed 1 km/s. This causes the leading edges to deteriorate during testing. Although the leading edges were repaired at several instances during the test campaign, the leading edge radius differs slightly across the inlet, and was determined as 0.2 ± 0.05 mm. A perfect fit between the location of the leading edge shock wave of the RANS sim-

ulation and the experiment was found after adjusting the leading edge radius in the computational grid to 0.25 mm, which is within the range of the measured value.

Another flow phenomenon, not fully captured by Fig. 10, is the separation zone upstream of the injector, represented by the hot region near the wall. The separation zone, which extents 25 mm upstream of the injector, induces a weak separation shock shown on both Fig. 6 and 10. To capture the separation size and shape well with RANS, the developing boundary layer on the compression ramp has to be in a laminar state. The separation exhibits laminar characteristics, judging from its size. This methodology was seen here to produce the best results for the comparison with experimental data. The Reynolds number and the Mach number at the edge of the boundary layer near the separation zone are roughly 6.6×10^5 and 5.8, respectively. According to Anderson [15], the typical transition Reynold number at Mach 5.8 is roughly 2×10^6, which furthermore justifies the assumption of a laminar boundary layer upstream of the injector.

The main flow features of the experiment are clearly shown in Fig. 10. The jet incident shock resulting from the strong over-expansion of the hydrogen jet is visualised by the temperature increase over the shock boundary. The low temperature region downstream of the injector represents the cold hydrogen-air mixture. The bow shock resulting from the hydrogen injection process, increases the post shock temperatures until the gas is cooled down due to expansion waves and the mixing process with cool hydrogen. Two distinct hot temperature patterns emerge in the post-bow-shock region, which are caused by the bow-shock itself and the bow-shock leading-edge-shock interaction. These regions are well suited for the comparison between experimental and computational results due to their distinct shape and temperature profile. Fig. 11 shows the direct translational temperature comparison of the computational and the experimental results. It can be clearly seen that the translational

freestream temperature is captured very well, resulting in relative errors smaller than 10 % . The post-leading-edge shock temperature matches the experiments as well. Even the size and shape of the separation could be captured, but the temperatures within the separation show discrepancies of up to 50 %. Above the jet incident shock and past the bow shock, two distinct high temperature regions develop, whose shape and temperatures are captured well with RANS ($\Delta T_{rot} \lesssim 10\%$) as shown in Fig. 11. The shape of the bow shock fits the experiment, but its position is slightly shifted upstream, compared to the experimental result. This is due to the uncertainty in the hydrogen mass flux, which arises from the fact that the plenum temperature is not directly measured. The region downstream of the jet incident shock near the wall shows good agreement as well. With increasing wall normal distance, however, the discrepancies increase, due to hydrogen mass fractions approaching 100%. This reduces the number of available NO molecules used for the temperature measurements, which results in large measurement uncertainties as shown in Fig. 8. Furthermore, the hydrogen-air shear layer is represented by a distinct line in RANS, which is due to the fact that unsteadiness cannot be resolved in the steady solution. This inhibits mass transport of cold hydrogen in the upper, and hot air in the lower regions, of the flow domain, thus the temperature blending is not well modeled.

3   Conclusions

The linear two-line thermometry technique has been used to measure ensemble-averaged temperatures of a sonic jet interacting with a hypersonic crossflow. Three electronic transitions were identified to cover a wide temperature range of 150–800 K giving relative uncertainties of 10–15 % in the freestream and 15–25 % in the regions behind the leading edge shock wave as well as the region behind the jet interaction shock wave. Uncertainties are higher where large-scale turbulence dominates the local flow, which is the case for the separated region upstream of the interaction shock as well as the mixing region downstream of the in-
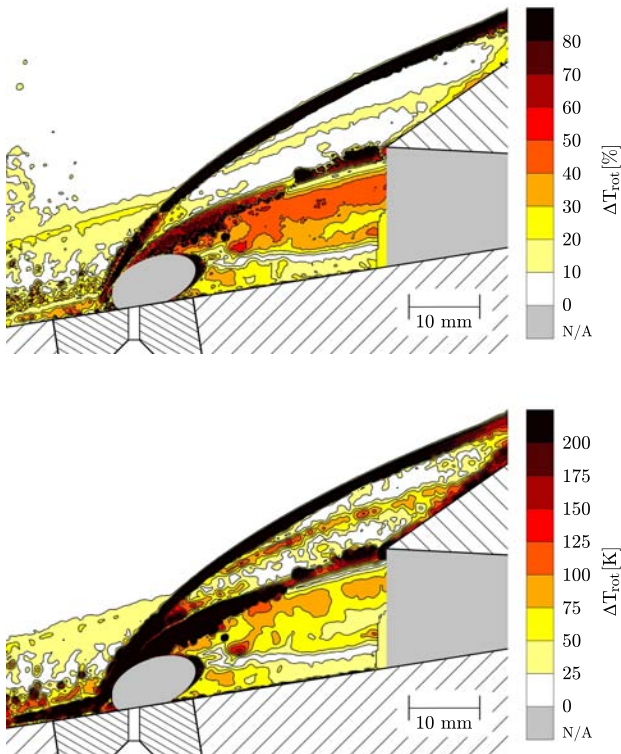
Fig. 11 : Relative (top) and absolute (bottom) temperature difference of RANS simulation to experimentally measured temperatures (Fig. 7).

jection port.

Good agreement is found between the experimental and numerical results. In particular, the quantitative agreement in large regions of the flow domain is good considering the fact that an unsteady flowfield was modeled employing steady RANS. The quality of simulation should, however, be improved in the separation zone upstream of the injector and in the hydrogen-air mixing and vortex-shedding region. This requires the usage of numerical methods that are capable of resolving unsteady flow phenomena, such as large-eddy simulations.

Acknowledgments

References

[1] R. K. Hanson, J. Seitzman, and P. Paul. Planar laser-fluorescence imaging of combustion gases. *Applied Physics B: Photophysics and Laser Chemistry*, 50:441–454, 1990.

[2] A. F. P. Houwing, J. L. Palmer, M. C. Thurber, S. D. Wehe, R. K. Hanson, and R. R. Boyce. Comparison of planar fluorescence measurements and computational modeling of shock-layer flow. *AIAA Journal*, 34(3):470–477, 1996.

[3] P. C. Palma, P. M. Danehy, and A. F. P. Houwing. Fluorescence imaging of rotational and vibrational temperature in a shock tunnel nozzle flow. *AIAA Journal*, 41(9):1722–1732, 2003.

[4] D. Müller, W. Triebel, A. Bochmann, G. Schmidl, D. Eckardt, A. Burkert, J. Röper, and M. Schwerin. *Two-dimensional concentration and temperature measurements in extended flames of industrial burners using PLIF*. in Optical Diagnostics for Fluids, Solids, and Combustion II, Farrell, P. V., Chiang, F. P., Mercer, C. R. and Shen, G. (eds), SPIE, Bellingham, USA, 2003.

[5] S. Brieschenk, S. O'Byrne, and H. Kleine. *PLIF Rotational Thermometry on a Scramjet Inlet with Fuel Injection*. 6th Australian Conference on Laser Diagnostics in Fluid Mechanics and Combustion, Canberra, 2011.

[6] NACA Ames. *Equations, tables and charts for compressible flow*. Report 1135, NACA Ames Aeronautical Laboratory, Moffett Field, USA, 1953.

[7] M. K. McIntosh. *Computer program for the numerical calculation of frozen and equilibrium conditions in shock tunnels*. Report, Australian National University, 1968.

[8] I. M. Vardavas. Modelling reactive gas flows within shock tunnels. *Australian Journal of Physics*, 37:157–177, 1984.

[9] J. Luque and D. R. Crosley. Transition prob-

abllites and electronic transition moments of the $A^2\Sigma^+ - X^2\Pi$ and $D^2\Sigma^+ - X^2\Pi$ systems of nitric oxide. *Journal of Chemical Physics*, 111(16):7405–7415, 1999.

[10] T. J. McGee, G. E. Miller, J. Burris, and T. J. McIlrath. Fluorescence branching ratios from the $A^2\Sigma^+$ (v'=0) state of NO. *Journal of Quantitative Spectroscopy and Radiative Transfer*, 29(4):333–338, 1983.

[11] I. Nompelis, T. W. Drayna, and G. V. Candler. *Development of a Hybrid Unstructured Implicit Solver for the Simulation of Reacting Flows Over Complex Geometries*. 34th AIAA Fluid Dynamics Conference and Exhibit, Portland, USA, 2004.

[12] P. R. Spalart and S. R. Allmaras. *A one-equation turbulence model for aerodynamic flows*. 30th AIAA Aerospace Sciences Meeting and Exhibit, Reno, USA, 1992.

[13] C. Park. *Nonequilibrium Hypersonic Aerothermodynamics*. John Wiley and Sons, New York, USA, 1989.

[14] H. S. Pergament. *A theoretical analysis of non-equilibrium hydrogen-air reactions in flow systems*. AIAA/ASME Hypersonic Ramjet Conference, Naval Ordnance Laboratory, White Oak, USA, 1963.

[15] J. D. Anderson. *Hypersonic and High-Temperature Gas Dynamics, 2nd Edition*. AIAA, Reston, USA, 2006.

Copyright Statement